

Feedback-Assisted Quantum Search by Continuous-Time Quantum Walks

Alessandro Candeloro,* Claudia Benedetti, Marco G. Genoni, and Matteo G. A. Paris

The quantum search of a target node on a cycle graph by means of a quantum walk assisted by continuous measurement and feedback are addressed. Unlike previous spatial search approaches, where the oracle is described as a projector on the target state, a dynamical oracle implemented through a feedback Hamiltonian is considered. The idea is based on continuously monitoring the position of the quantum walker on the graph and then applying a unitary feedback operation based on the information obtained from measurement. The feedback changes the couplings between the nodes and it is optimized at each time via a numerical procedure. The stochastic trajectories describing the evolution for graphs of dimensions up to $N = 15$ are numerically simulated, and the performance of the protocol is quantified via the average fidelity between the state of the walker and the target node. Different constraints on the control strategy are discussed. For unbounded controls, the protocol is able to quickly localize the walker on the target node. How the performance is lowered by posing an upper bound on the control couplings is then discussed. Finally, it is shown how a digital feedback protocol seems in general as efficient as the continuous bounded one.

1. Introduction

Quantum walks are used to model the evolution of a quantum particle, or excitation, over a discrete set of positions. If the walker dynamics is continuous in time, that is, time is a real positive parameter, we talk about continuous-time quantum walk (CTQW).^[1–3] In many contexts, quantum walks show a quantum advantage with respect their classical counterpart, by allowing a speed-up in completing certain tasks. Examples are found in quantum computation^[4–6] and quantum algorithms.^[7–17] Since a CTQW evolves over a graph, it is strongly related to applications over networks, including quantum spatial search,^[18–24] quantum

routing,^[25–27] quantum transport, and state transfer.^[28–30] The ability to redirect or control information over a graph in an efficient way is essential to develop protocols involving quantum networks and to deal with a large amount of structured data. To this aim, we develop a protocol to guide the walker toward a target node on a graph by exploiting the tools of quantum control.

The theory of quantum control^[31] addresses the problem of preparing a quantum system in a desired quantum state or with some desired quantum properties. In quantum feedback-control strategies the quantum system under control is measured (typically continuously in time) and the information acquired is exploited in order to optimize a feedback operation on the system itself. This kind of strategies has been studied in great detail, in particular with the aim of generating quantum states with non-classical properties such as squeezing or entanglement^[32–49] or to cool optomechanical systems toward their ground

states, with the experimental results recently demonstrated in refs. [50–52].

In this article, we propose a novel approach to quantum search on graphs and establish a new and unexplored line of research combining CTQWs with quantum feedback-control protocols. In our system, the walker is interacting with an environment that is continuously monitored. As a result, the system evolution is a quantum stochastic trajectory and, based on the result of the measurement, a feedback protocol is applied. We will prove that it is possible to drive the walker toward a target state by optimizing the corresponding target fidelity at each step. Our method differs from other methods that have been developed since it allows the walker to be guided continuously to the target node. In the standard spatial search protocol the oracle is described as a projector operator onto the target state. With our approach we modify this paradigm. We consider a *dynamical* oracle encoded in the feedback operation. This means that the final projective measurement on the walker, to be performed at any time t after a certain threshold time t_{th} , has a high probability of success. In particular, we find that once the walker reaches the target node it remains stuck in it thanks to the feedback operation. This lift the burden of performing a final measurement at a very specific time, by allowing us to measure the walker position at any time $t \geq t_{th}$.

The manuscript is organized as follows: in Section 2 and in Section 3 we give a brief introduction to continuous-time

A. Candeloro, C. Benedetti, M. G. Genoni, M. G. A. Paris
Quantum Technology Lab
Dipartimento di Fisica Aldo Pontremoli
Università degli Studi di Milano
Milano I-20133, Italy
E-mail: alessandro.candeloro@unimi.it
M. G. Genoni, M. G. A. Paris
INFN
Sezione di Milano
Milano I-20133, Italy

 The ORCID identification number(s) for the author(s) of this article can be found under <https://doi.org/10.1002/qute.202200093>

DOI: 10.1002/qute.202200093

quantum walks, and to continuously monitored quantum systems and unitary (measurement-based) feedback strategies, respectively. In Section 4, we introduce our search scheme and we describe the idea behind our feedback protocol. In Section 5 we analyze our results for the different control strategies we have considered, while we conclude the manuscript in Section 6 with some remarks and outlooks.

2. Quantum Walks and Spatial Search on Graphs

A continuous-time quantum walk describes the continuous motion of a quantum particle over a discrete set of positions. Underlying every walk there is a graph G , which is described as a pair $G = (V, E)$ where $V = \{0, 1, \dots, N-1\}$ is the set of vertices and E is the set of undirected edges, that is, all the pairs of adjacent vertices in V . For a CTQW, the vertices represent the positions that the particle can occupy while the edges encode all the possible paths that a walker can move across. We denote the order of the graph as the number of nodes $N = |V|$. We restrict our discussion to regular graphs, with no loops nor multiple edges. All this information determines the topology of the graph and is encoded in the adjacency matrix A . In the position basis $\mathcal{B}_p = \{|k\rangle\}_{k=0}^{N-1}$, this is given by the matrix elements

$$\langle i|A|j\rangle = A_{ij} = \begin{cases} 1 & \text{if } (i,j) \in E \\ 0 & \text{if } (i,j) \notin E \end{cases} \quad (1)$$

For example, in the case of a cycle graph the only non-zero elements are A_{jk} and A_{kj} satisfying the condition $k = (j+1) \bmod N$, with $j = 0, \dots, N-1$. Associated to A there is a Laplacian matrix, defined as $L = D - A$. Here D is a diagonal matrix, with $\langle k|D|k\rangle = d_k = \sum_{j=0}^{N-1} A_{kj}$ the degree of the k th vertex. The Laplacian matrix is promoted to be the generator of the quantum dynamics and the physical origin behind this choice is the correspondence between L and the discretized kinetic operator for regular lattices.^[53] Hence, the quantum walker Hamiltonian is $H = \gamma L$, where the parameter $\gamma > 0$ is the hopping rate between the nodes and it accounts for the energy scale of the system. The generic state of the CTQW at time t is a superposition over the vertices $|\psi(t)\rangle = \sum_k a_k |k\rangle$ with $a_k = \langle k|e^{-iHt}|\psi_0\rangle$ and $|\psi_0\rangle$ the initial state of the walker. Throughout the paper we set $\hbar = 1$. In the case of regular graphs, the matrix D is proportional to the identity operator, thus making the evolutions generated by L and A equivalent. Before proceeding, we want to remark that using L as the dynamics generator is only one of the possible (infinitely many) choices for a Hamiltonian. Indeed any Hermitian operator, which respects the topology of the graph, can be used as a legit CTQW Hamiltonian.^[53–57]

One application of CTQWs is the spatial search algorithm. The goal is to exploit the coherent evolution of a quantum walker to find a marked vertex on a graph faster than its classical counterpart. In the quantum spatial search of a marked node $|w\rangle$, the walker evolves under the Hamiltonian

$$H_S = \gamma L - |w\rangle\langle w| \quad (2)$$

where γ is a real parameter and the operator $|w\rangle\langle w|$ is the oracle Hamiltonian that is, a projector onto the target state. The

walker is usually initialized in the uniform superposition of all nodes

$$|\psi_0\rangle = \frac{1}{\sqrt{N}} \sum_{k=0}^{N-1} |k\rangle \quad (3)$$

with no bias toward the target state. The algorithm is successful if the probability of finding the target node $p_w(t_s) = |\langle w|e^{-iH_S t_s}|\psi_0\rangle|^2$ is as close as 1 as possible in a time $t_s = \mathcal{O}(\sqrt{N})$. It was shown that a \sqrt{N} speedup can be obtained for specific topologies, such as the complete and hypercube graphs and $(d > 4)$ -dimensional lattices.^[18,58] Later studies proved fast search for different kinds of graphs^[59–64] and a comprehensive analysis of the algorithm's performances was carried out in ref. [65], which recovers previous graph-dependent results as special cases. It is worth mentioning here that considering different oracle operators, such as those which modify the edges connected to the target node, allows to reach a search time $t_s = \mathcal{O}(\sqrt{N \ln N})$ in 2D ($d = 2$) lattices, by building Hamiltonians that exhibit Dirac points in their dispersion relation.^[20,66] Since low dimensional lattices, such as the cycle graph, do not sustain fast search with the standard algorithm defined by Hamiltonian Equation (2), novel strategies must be envisaged to boost the spatial search on these structures. We report in Appendix A the success probability of the standard search algorithm on the cycle graph to set a benchmark for our approach.

3. Continuous Monitoring and Feedback Control

3.1. Continuously Monitored Quantum Systems

We here provide a very basic introduction to continuously monitored quantum systems. We refer to the following references^[31,67,68] for a more detailed introduction and for the derivation of the formulas provided in this section. We assume that the quantum system under exam interacts with a large Markovian environment described by a train of input bosonic operators $\hat{a}_j(t)$ satisfying the canonical commutation relation $[\hat{a}_j(t'), \hat{a}_k^\dagger(t)] = \delta_{jk} \delta(t - t')$. The interaction with the system is then given in terms of the time-dependent interaction Hamiltonian

$$\hat{H}^{\text{int}}(t) = i \sum_j \sqrt{\kappa_j} (\hat{c}_j \hat{a}_j^\dagger(t) - \hat{c}_j^\dagger \hat{a}_j(t)) \quad (4)$$

in which κ_j represent the coupling strengths, while \hat{c}_j are operators acting on the system Hilbert space (one should also notice that the parameter t in the operators $\hat{a}_j(t)$ is just a label denoting the time at which each operator is interacting with the quantum system via the Hamiltonian). We also assume that the environmental modes $\hat{a}_j(t)$ can be measured continuously in time, just after the interaction, in order to gain information on the state of the system itself. Notice that the interaction with the environment can be either considered already present, and that some degree of control on this environment is achievable in order to perform such a measurement, or that such an interaction can be effectively engineered with the purpose of weakly monitoring the system. Both these approaches are nowadays pursued efficiently in different physical platforms, in particular in circuit

QED^[69–73] and in optomechanical systems.^[74–78] It is known that in quantum mechanics a measurement modifies the state of the quantum system that is (directly or indirectly) measured, and that the corresponding *conditional state* will depend both on the kind of measurement performed and on the outcome of the measurement. We will focus on continuous homodyne detection of the environmental modes with monitoring efficiencies η_j , corresponding to a set of continuous photocurrents

$$dY_t^{(j)} = \sqrt{\eta_j \kappa_j} \text{Tr} \left[(\hat{c}_j + \hat{c}_j^\dagger) \rho^c \right] dt + dW_t^{(j)} \quad (5)$$

where $dW_t^{(j)}$ denotes the *innovation*, that is the difference between the result of the measurement $dY_t^{(j)}$ and the expected results, and mathematically correspond to independent Wiener increments satisfying $dW_t^{(j)} dW_t^{(k)} = \delta_{jk} dt$. The evolution of the quantum state $\rho^c(t)$ conditioned on the photocurrents $dY_t^{(j)}$ is then given by the following stochastic master equation (SME)

$$d\rho^c = -i[\hat{H}_s, \rho^c(t)]dt + \sum_j \kappa_j D[\hat{c}_j] \rho^c(t) dt + \sum_j \sqrt{\eta_j \kappa_j} H[\hat{c}_j] \rho^c(t) dW_t^{(j)} \quad (6)$$

where \hat{H}_s is the Hamiltonian describing the evolution of the quantum system only, and where we have introduced the two following superoperators

$$D[\hat{c}] \bullet = \hat{c} \bullet \hat{c}^\dagger - (\hat{c}^\dagger \hat{c} \bullet + \bullet \hat{c}^\dagger \hat{c})/2 \quad (7)$$

$$H[\hat{c}] \bullet = \hat{c} \bullet + \bullet \hat{c}^\dagger - \text{Tr}[(\hat{c} + \hat{c}^\dagger) \bullet] \bullet \quad (8)$$

The continuous outcomes of the photocurrents $\{dY_t^{(j)}\}$ thus define a particular conditional trajectory for the conditional state of the quantum system. By averaging over all the possible trajectories, that is, over all the possible outcomes of the measurements, we obtain the evolution of the unconditional state $\rho^u = \mathbb{E}_{\text{traj}}[\rho^c]$ that, by exploiting the property $\mathbb{E}_{\text{traj}}[dW_t^{(j)}] = 0$, is a Markovian master equation in the Lindblad form

$$\frac{d\rho^u}{dt} = -i[\hat{H}_s, \rho^u(t)] + \sum_j \kappa_j D[\hat{c}_j] \rho^u(t) \quad (9)$$

The evolution of the conditional states described by the SME in Equation (6) can be equivalently described via the formula^[79,80]

$$\rho^c(t+dt) = \frac{\hat{M}_{dy_t} \rho^c(t) \hat{M}_{dy_t}^\dagger + \sum_j (1 - \eta_j) \hat{c}_j \rho^c(t) \hat{c}_j^\dagger dt}{\text{Tr}[\hat{M}_{dy_t} \rho^c(t) \hat{M}_{dy_t}^\dagger + \sum_j (1 - \eta_j) \hat{c}_j \rho^c(t) \hat{c}_j^\dagger dt]} \quad (10)$$

where we have introduced the family of Kraus operators

$$\hat{M}_{dy_t} = \mathbb{I} - i\hat{H}_s dt - \sum_j \left(\frac{\kappa_j}{2} \hat{c}_j^\dagger \hat{c}_j dt - \sqrt{\eta_j \kappa_j} \hat{c}_j dY_t^{(j)} \right) \quad (11)$$

with $\mathbf{dy}_t = \{dY_t^{(1)}, \dots, dY_t^{(K)}\}$ denoting the vector of the outcomes of the K measurements channels.

In our protocol we consider an initial pure state and perfect monitoring efficiency, that is, $\eta_j = 1$ for all channels. Under these assumptions the conditional evolution is described by a stochastic Schrödinger equation, or equivalently via the Kraus operators as follows

$$|\psi^c(t+dt)\rangle = \frac{\hat{M}_{dy_t} |\psi^c(t)\rangle}{\sqrt{\langle \psi^c(t) | \hat{M}_{dy_t}^\dagger \hat{M}_{dy_t} | \psi^c(t) \rangle}} \quad (12)$$

3.2. Unitary Quantum Feedback

In addition to conditioning the evolution of the quantum state, the outcomes of the measurement performed can in principle be exploited to further modify the dynamics of the system. In this respect, here we briefly introduce unitary measurement-based quantum feedback. The idea is that, once the measurement outcomes \mathbf{dy}_t are obtained, one performs a unitary operation $\hat{U}_{fb}(\mathbf{dy}_t)$ on the quantum state, typically optimized in order to achieve a certain goal as, for example, the preparation of a certain target quantum state. This unitary operation may depend only on the last measurement outcomes, or on the whole history of outcomes, and thus on the whole trajectory of the conditional state. In the first instance one talks about Markovian quantum feedback and one can derive a corresponding Markovian feedback master equation.^[31,33] In this work we will focus on the second kind of feedback, and thus our feedback strategy will be optimized by knowing both the last measurement outcomes and the conditional state $|\psi^c(t)\rangle$ (and as a consequence the whole measurement history). In order to obtain the corresponding evolution, we exploit the formulas involving the Kraus operators. In particular, if the feedback operation is performed after the measurement, by assuming unit measuring efficiency, initial pure states and no-delay between measurement and feedback, the conditional state at each instant is described via the formula

$$|\psi^{fb}(t+dt)\rangle = \frac{\hat{U}_{fb} \hat{M}_{dy_t} |\psi^{fb}(t)\rangle}{\sqrt{\langle \psi^{fb}(t) | \hat{M}_{dy_t}^\dagger \hat{M}_{dy_t} | \psi^{fb}(t) \rangle}} \quad (13)$$

This formula is particularly useful for our numerical approach where one needs to substitute the time differential dt with a finite but small time increment Δt , while the Wiener increment $dW_t^{(j)}$ must be replaced by a Gaussian random variable $\Delta W_t^{(j)}$ with zero mean and variance Δt . The finite increments to the measurement records are

$$\Delta Y_t^{(j)} = \sqrt{\kappa_j} \langle \psi^c(t) | (\hat{c}_j^\dagger + \hat{c}_j) | \psi^c(t) \rangle \Delta t + \Delta W_t^{(j)} \quad (14)$$

Due to the finite nature of Δt , the deterministic identity $\Delta W_t^{(j)2} = \Delta t$ is no longer satisfied, thus corrections must be considered. This is accomplished by adding an extra term, known as Euler–Millstein correction,^[80] in the Kraus operators that now read

$$\hat{M}_{\Delta y_t} = \mathbb{I} - i\hat{H}_s \Delta t - \sum_j \left(\frac{\kappa_j}{2} \hat{c}_j^\dagger \hat{c}_j \Delta t - \sqrt{\kappa_j} \hat{c}_j \Delta Y_t^{(j)} - \frac{\kappa_j}{2} \hat{c}_j^2 (\Delta Y_t^{(j)2} - \Delta t) \right) \quad (15)$$

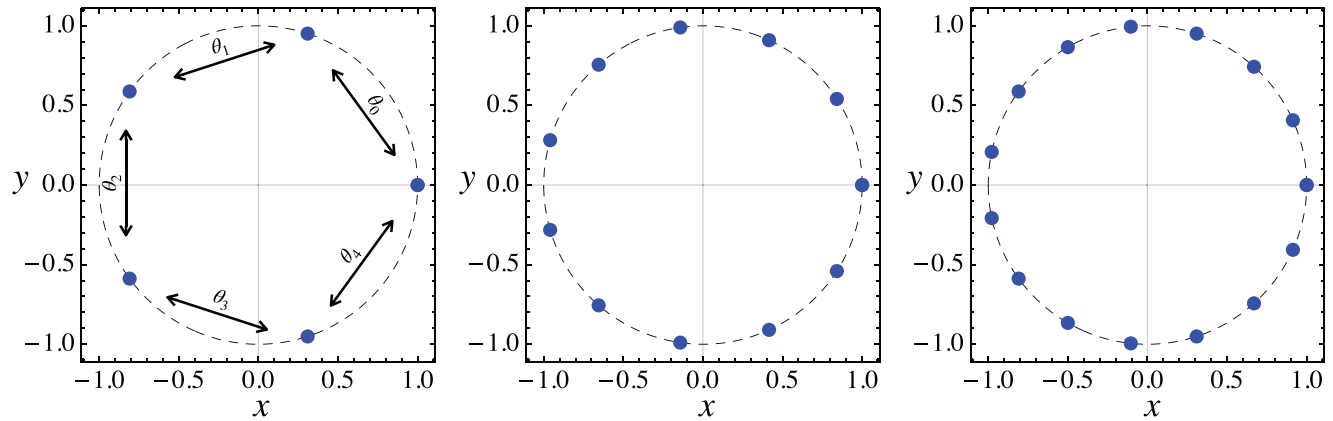


Figure 1. Cycle graph embedded in a plane on a circle of unit radius. Left panel: $N = 5$; central panel: $N = 11$; right panel: $N = 15$.

4. Quantum Search Assisted by Feedback

Our idea is to continuously monitor the position of a quantum walker during its evolution on a cycle graph, and then to use this information to apply feedback unitary operations as a dynamical oracle with the aim of finding a particular target node. The walker is initially prepared in the uniform superposition of all nodes of the graph as in Equation (3). The first step is to describe the continuous monitoring. In particular we assume to be able to couple our system to two different environments via the following jump operators

$$\hat{c}_1 = \hat{x} = \sum_{k=0}^{N-1} \cos\left(\frac{2\pi k}{N}\right) |k\rangle\langle k| \quad (16)$$

$$\hat{c}_2 = \hat{y} = \sum_{k=0}^{N-1} \sin\left(\frac{2\pi k}{N}\right) |k\rangle\langle k| \quad (17)$$

whose eigenvalues exactly correspond to the coordinates of the position of the N nodes of the graph, corresponding to equally spaced points on a unit radius ring centered on $(0,0)$ in the (x, y) plane (see **Figure 1** for cycle graphs with $N = 5, 11, 15$). By performing continuous homodyne detections one obtains two photocurrents (Equation (5)) whose average values are indeed proportional to the expectation values of the operators \hat{x} and \hat{y} on the conditional state ρ^c . We show in Appendix B that the unconditional evolution, corresponding to the master Equation (9) with the cycle graph Hamiltonian $H_S = \gamma L$ and jump operators (Equations (16) and (17)), leads to a symmetric dephasing-like evolution in the position basis, thus reflecting the translation invariance of the graph's nodes and further validating our choice. In Appendix C we also mention an alternative choice for the jump operator, that is, the single non-Hermitian jump operator

$$\hat{c}_0 = \sum_{k=0}^{N-1} e^{i2\pi k/N} |k\rangle\langle k| \quad (18)$$

that satisfies the properties discussed above. We show that the results are comparable with the one obtained via the two Hermitian jump operators \hat{c}_1 and \hat{c}_2 .

The second step is to define our feedback strategy. We parametrize the unitary feedback operator as

$$\hat{U}_{fb}(\theta) = e^{-i\hat{H}_{fb}(\theta)t} \quad (19)$$

where, in general, we assume to have a finite number of control parameters $\theta = \{\theta_k\}$ corresponding to a set of control operators $\{\hat{h}_k\}$, such that the feedback Hamiltonian reads

$$\hat{H}_{fb}(\theta) = \sum_k \theta_k \hat{h}_k \quad (20)$$

The definition of the control operators is indeed crucial. Two natural choices can be considered: the first one is to choose the on-site projectors, that is, $\hat{h}_k^{(os)} = |k\rangle\langle k|$. However preliminary numerical simulations show that this choice is in general not efficient. In order to understand why this is the case, one can for example observe that, being $\{|k\rangle\}$ eigenstates of the control operators above, if the walker during the evolution happens to be in a node $|k\rangle$ different from the target, the unitary operation will not be able to change its state and thus the feedback is useless for our purposes. The second natural choice is to consider the hopping operators

$$\hat{h}_k^{(hop)} = |k\rangle\langle k+1| + |k+1\rangle\langle k| \quad (21)$$

with the usual boundary condition $|N\rangle \equiv |0\rangle$. This set of feedback control operations represents the ability of controlling each coupling between adjacent nodes individually.

Finally, one needs to decide how to optimize the feedback operation, that is the set of control parameters θ , in order to find the target node on the graph. This is typically done by defining a reward function $\Lambda(|\psi^{fb}\rangle)$, that in our case naturally corresponds to the fidelity between the conditional state after the feedback operation $|\psi^{fb}\rangle$ in Equation (13), and the target state (that we will hereafter denote as $|0\rangle$), that is,

$$\Lambda(|\psi^{fb}(t)\rangle) = \mathcal{F}_{|0\rangle}(|\psi^{fb}(t)\rangle) = |\langle 0|\psi^{fb}(t)\rangle|^2 \quad (22)$$

We will thus choose the parameters θ as the ones maximizing the fidelity at each step of the trajectory. The same figure of merit will be then used in order to assess the performance of our protocol.

We will indeed numerically evaluate

$$\bar{F}_{|0\rangle} = \mathbb{E}_{\text{traj}}[\bar{F}_{|0\rangle}(|\psi^{\text{fb}}(t)\rangle)] \quad (23)$$

that is the fidelity averaged over all the possible trajectories conditioned by the continuous monitoring.

5. Results

In the following, we present our main results, dividing them in three different settings: in Section 5.1 we address the numerical optimization of the feedback operation with unbounded control parameters, that is, without posing any bound on the search domain for the parameters $\{\theta_i\}$. Then, in Section 5.2 we consider numerical optimization of the feedback but with a bounded domain, that from the physical point of view may represent constraints on the physical implementation of the feedback operations. In Section 5.3 we study the case of *digital feedback*,^[81] in which the value of the feedback couplings are not only bounded, but can take values only from a discrete set (one should notice that unlike previous examples of digital feedback,^[81] we still have a continuous measurement output, and only the feedback operations are discrete). In all these examples we consider the system initially prepared in the quantum state defined in Equation (3), corresponding to the uniform superposition over the N nodes of the graph.

The algorithm we used to numerically optimize the feedback couplings is provided by the SciPi library, and in particular the `scipy.optimize.minimize` function.^[82] The method used for the different strategies are the following: for the unbounded optimization (Section 5.1) we use the BFGS method; for the bounded optimization (Section 5.2) we used the L-BFGS-B method. Differently, the method used for digital feedback (Section 5.3) is a brute force one, that is, we consider all the possible combinations of the finite discrete values and we select the optimal one.

We remark that we have also investigated the scenario with a single feedback Hamiltonian controlling collectively all the couplings via a single parameter θ , that is, via the Hamiltonian $\hat{H}_{\text{fb}} = \theta \sum_k \hat{h}_k^{(\text{hop})}$. However, as we show in Appendix E, this kind of feedback is not particularly efficient for our purposes.

5.1. Numerical Optimization with Unbounded Controls

We here show the results of our protocol when considering a feedback operation via the control operators introduced in Equation (21) and optimized control parameters $\{\theta_k\}$ with unbounded domain. A remark is in order here: the first attempt we have pursued was to follow the approach described by Martin et al. in refs. [45, 47], where the feedback operation is assumed to be infinitesimal, that is, via couplings written as

$$\theta dt = A d\mathbf{W} + B dt \quad (24)$$

where $\theta = (\theta_1, \dots, \theta_K)^T$ is the vector of the feedback couplings, $d\mathbf{W} = (dW_t^{(x)}, dW_t^{(y)})$ is the vector of the Wiener increments describing the measurement, while A and B , are respectively a $(N \times 2)$ -dimensional matrix and a 2D vector describing the feedback strategy. The optimization in this scenario could be done analytically if some conditions are fulfilled, as described in ref. [45]

(see Appendix E for further details on this method). However for our problem we verify that these conditions are never satisfied and thus a numerical optimization with unbounded couplings has to be performed.

The results are depicted in **Figure 2** for $N = 5, 11$, and 15 , where we observe that the protocol is particularly efficient in reaching the target state. In order to quantify the efficiency of our protocol, we fix a threshold value for the average fidelity $\bar{F}^{\text{th}} = 0.95$, such that whenever the reward function is larger than this threshold value, the target search is considered successful. This efficiency decreases as the size of the graph increases, although the threshold value is reached on rather small time scales $\gamma t < 1$. This is a great improvement with respect to the performance of the standard quantum spatial search algorithm, reported in Appendix A, where the success probability never reaches the threshold value (see Figure A1 for a comparison).

In Figure 2 we also consider the average feedback coupling $\bar{\theta}_0$ between nodes $|0\rangle$ and $|1\rangle$ and the coupling $\bar{\theta}_1$ between nodes $|1\rangle$ and $|2\rangle$ (see Figure 1 for reference): after an initial transient, the average value of the feedback couplings reaches an asymptotic value, meaning that the feedback operation is stable after having reached the target node. We notice that the average coupling $\bar{\theta}_0$, between nodes $|0\rangle$ and $|1\rangle$, tends to the asymptotic value $\bar{\theta}_0 \rightarrow -\gamma$. In fact, when the protocol has *almost* localized the walker in the desired node, the role of the feedback is to try to stop the dynamics by nullifying the corresponding couplings in the Hamiltonian. We have also numerical evidence that, within numerical noise, the average feedback couplings are symmetric with respect to the x -axis, that is, $\bar{\theta}_0 = \bar{\theta}_{N-1}$, $\bar{\theta}_1 = \bar{\theta}_{N-2}$, etc., in the configuration in which the target node is placed in $(1,0)$, see Figure 1. The average feedback couplings reported in Figure 2 show however large fluctuations, especially $\bar{\theta}_1$, suggesting that in some trajectories larger values of the optimal couplings are chosen by the optimization algorithm. We propose two possible justifications for this behavior: i) the first one is based on the stochasticity of the single random trajectory, that is, there might be a time-step in which the measurement project the state far away from the target node, and thus a large correction is needed; ii) the second one is based on the shape of the landscape functions of the feedback couplings for a single trajectory. One can indeed observe that these landscape functions are periodic and thus have many local and equal maxima that can be reached by different values of the feedback couplings. The large fluctuations thus may arise from the fact that the algorithm does not always choose the maximum in the neighborhood of the maximum found at the previous step (further details on the couplings' landscape functions are given in Appendix D).

5.2. Numerical Optimization with Bounded Controls

As we have seen in the previous section, not only numerical optimization of the feedback strategy is necessary, but also large absolute values of the feedback couplings might be needed to perform an efficient search. Hence, to test the limits of our protocol, we consider the case where the feedback couplings θ belong to a bounded domain. In this case each θ_k can take values from the interval $[-\xi\gamma, \xi\gamma]$, where we introduced the bounding (dimensionless) parameter ξ that quantifies the range of values admitted for

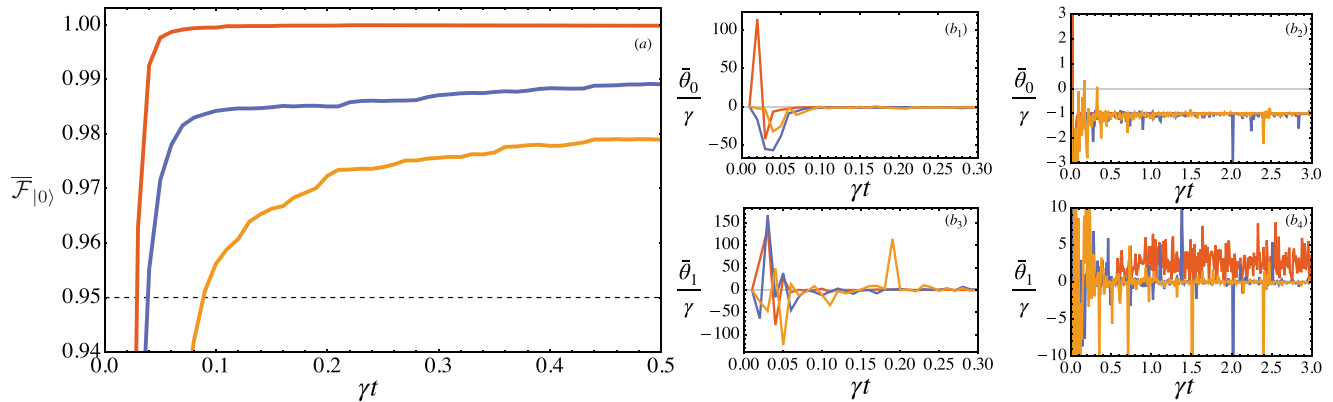


Figure 2. Results for multiple feedback control Hamiltonians $\hat{h}_k^{(\text{hop})}$ defined in Equation (21). a): average reward function $\bar{F}_{|0\rangle}$ as a function of time (black dashed line: threshold $F^{\text{th}} = 0.95$). b₁–b₄) Averaged feedback couplings $\bar{\theta}_k$, corresponding to the k th Hamiltonian in Equation (20)). Short time behavior: (b₁, b₃); time-asymptotic behavior: (b₂, b₄). Red line: $N = 5$; blue line: $N = 11$; orange line: $N = 15$. Other parameters: $\eta = 1$, $dt = 0.01$, number of stochastic trajectory $N_{ij} = 5000$.

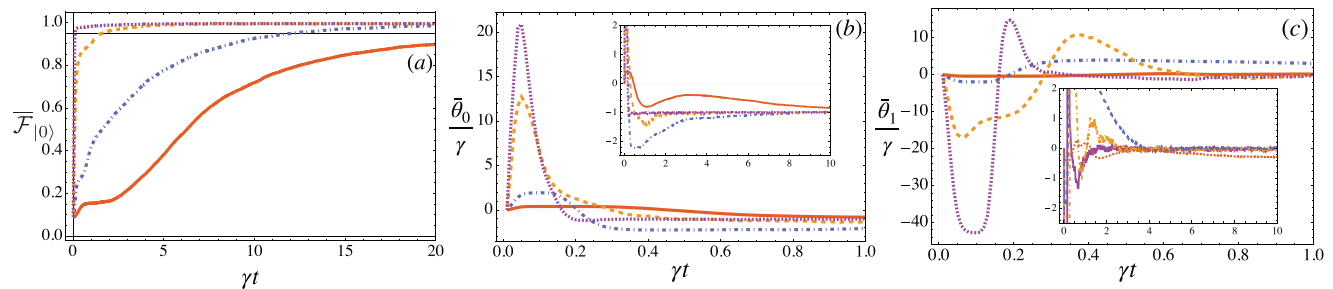


Figure 3. Results for multiple feedback Hamiltonians $\hat{h}_k^{(\text{hop})}$ with bounded control parameters θ and for a graph with $N = 11$ nodes. a) Average reward function $\bar{F}_{|0\rangle}$ as a function of time (black thick line: threshold $F^{\text{th}} = 0.95$); b,c) Average feedback coupling $\bar{\theta}_0$ and $\bar{\theta}_1$, respectively, as a function of time (short time behavior). Insets: Average feedback coupling $\bar{\theta}_0$ and $\bar{\theta}_1$ for a larger time t (asymptotic behavior). In all plots we used $\xi = 1$ (red thick line), $\xi = 5$ (blue dotted line), $\xi = 50$ (orange dashed line), $\xi = 100$ (purple dotted line), $\eta = 1$, $dt = 0.01$, number of stochastic trajectories $N_{ij} = 5000$.

the feedback couplings θ . We consider the bounding parameter $\xi \geq 1$. We have indeed numerical evidence that for $\xi < 1$, that is for feedback couplings smaller than the Laplacian parameter γ , the protocol fails. As we noticed in the example above, once the walker has been localized over the target the role of the feedback is to stop the dynamics and this effect cannot be achieved efficiently if in general $|\theta_0| < \gamma$.

The numerical results are provided in Figure 3 for $N = 11$ (the results are qualitatively similar also for $N = 5$ and $N = 15$), and for different values of ξ ranging between $\xi = 1$ and $\xi = 100$. As expected, as ξ grows, the efficiency of the protocol improves, that is, the minimum time t_{th} required to reach the threshold F^{th} decreases on average. Moreover, even for small values of ξ , this protocol is able to identify the target node with higher probability than the standard quantum algorithm in the same time interval, see Appendix A.

The decreasing of the optimal time γt_{th} for increasing values of ξ can also be seen from Figure 4, where we plot the ratio of $\gamma t_{\text{th}}/F^{\text{th}}$, a quantity that corresponds to the effective time necessary to reach the target on average.^[83] We observe that this quantity in general quantitatively depends on the chosen threshold value F^{th} but it gives always the same qualitative behavior. We

see that above a certain value of ξ , the ratio reaches a minimum asymptotic value. Larger values of ξ are necessary to reduce the effective time $\gamma t_{\text{th}}/F^{\text{th}}$ when the size N is increased. From Figures 3 and 4, we notice that the order of magnitude of the t_{th} is larger if compared with the one obtained for the unbounded feedback (see Figure 2).

In Figure 3 we also report the average values of the feedback couplings $\bar{\theta}_0$ and $\bar{\theta}_1$. Differently from the unbounded controls scenario, here the noisy fluctuations are much smaller (again, for a more detailed discussion, we refer the reader to Appendix D), and we have numerical evidence that the time behavior of $\bar{\theta}_0$ and $\bar{\theta}_1$ is equal to their symmetric counterpart $\bar{\theta}_{10}$ and $\bar{\theta}_9$. The qualitative behavior of $\bar{\theta}_0$ is the same also for the other values of N and ξ considered: after a first positive peak, it follows a minimum and then a second maximum, which is smaller than the first, and eventually it tends to the finite asymptotically value $\bar{\theta}_0 \rightarrow -\gamma$, confirming our previous intuition. The situation is slightly different for $\bar{\theta}_1$, where for $N = 11$ and $N = 15$ there is a sequence of minima and maxima which asymptotically tend to a value close to 0 while for $N = 5$ the asymptotic values remains positive. This behavior leads to the observation that, for smaller graphs, the couplings θ_1 and θ_{N-2} are more relevant with respect to graphs with

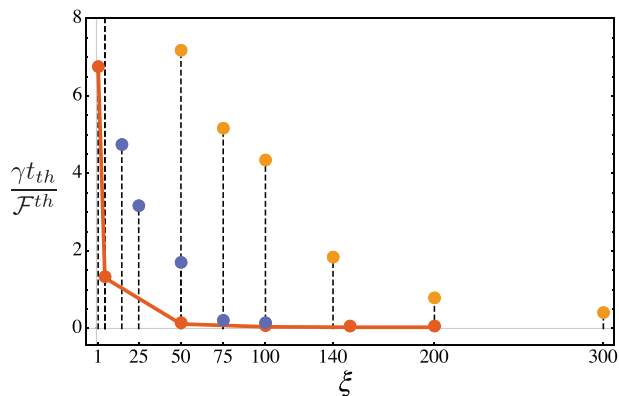


Figure 4. Plot of $\gamma t_{th}/F^{th}$ as a function of the bounding parameter ξ for different graph sizes: $N = 5$ (red line), $N = 11$ (blue line), and $N = 15$ (orange line). The value t_{th} is the time at which the $F^{th} = 0.95$ is reached on average. By changing the value of the threshold parameter F^{th} the qualitative behavior of the curves does not change and the values obtained for different ξ have the same order of magnitude. We used the same data and the same set of parameters of Figure 3.

a larger size. The other feedback couplings are not particularly interesting, since their average is approximately 0 everywhere, so we decide to not report them.

So far we have discussed only averaged results on a large number of trajectories. To understand in detail the behavior of the protocol, in **Figure 5** we report the results for a single stochastic trajectory with bounded domain for $N = 5$ with $\xi = 1$ and $N = 11$ with $\xi = 5$. During the transient evolution, when the feedback is driving the walker to the target node $|0\rangle$, the value of the reward function is particularly affected by the measurement. After reaching the threshold value, the feedback operation tries to keep the walker into the target vertex. However, the stabilization procedure is not given by constant values of the feedback couplings. Similar to what we have discussed in the previous section, this means that corrections are necessary also after having reached the target state with high fidelity. These corrections are responsible for the noise we see in the averaged feedback couplings reported in Figure 3. By inspecting the single trajectories, we also notice that most of the values taken by θ during the evolution are

either equal to 0 or to $\pm\gamma$. So it is worth exploring a scenario where the feedback couplings θ belong to discrete set of possible values.

5.3. Numerical Optimization with Digital Feedback Control

We now explore a digital feedback protocol, where the feedback control parameters θ are picked, at each time step, from a discrete number of values. We study this strategy only for a cycle graph of order $N = 5$ since the numerical algorithm we employed is particularly demanding.

First, we consider only three possible values for the couplings θ_k , belonging to the set $\{0, \pm\gamma\}$. In this case the optimization algorithm explores all the values of the reward function for all the possible combinations that the five feedback couplings θ may realize, that is, $5^3 = 125$ possible combination, and select the one that realizes the maximum $F_{|0\rangle}(\bullet)$. In the left panel of **Figure 6** we report the results obtained by repeating this algorithm at each step and averaging over $N_{ij} = 5000$ trajectories. We see that the threshold value of F_{th} is reached for a time $\gamma t_{th} = 6.40$, which is slightly larger than the value obtained via the continuous bounded protocol $\gamma t_{th} = 6.39$. Regarding the feedback couplings θ , their average values oscillate in the transient time, and after the threshold time t_{th} , they stabilize around asymptotic values. We found that approximately $\bar{\theta}_0 = \bar{\theta}_4 = -\gamma$, while $\bar{\theta}_1, \bar{\theta}_2$, and $\bar{\theta}_3$ correspond in general to positive values.

Then, we consider five possible values for the feedback couplings θ_k , belonging to the set $\{0, \pm\gamma, \pm\xi\gamma\}$, with ξ playing the same role of the bounding factor we introduced before. Here, we may consider the two extra switchers as a boosted feedback operation, that is, a larger coupling strength than the standard γ . In this case, the number of possible combination increase and it is equal to $5^5 = 3125$. The averaged results are reported in **Figure 6b** for $\xi = 5$ and for $N_{ij} = 5000$ trajectories. The threshold value is reached, on average, by the time $\gamma t_{th} = 1.12$, which in this case is slightly smaller than the continuous-bounded protocol threshold time $\gamma t_{th} = 1.24$. This result is indeed unexpected since the digital feedback is an instance of the strategies allowed by the continuous bounded domain. This suggests that all the algorithms we employed for the optimization of the continuous bounded domain are not particularly efficient in finding the optimal values of the parameters θ , while the brute-force spanning

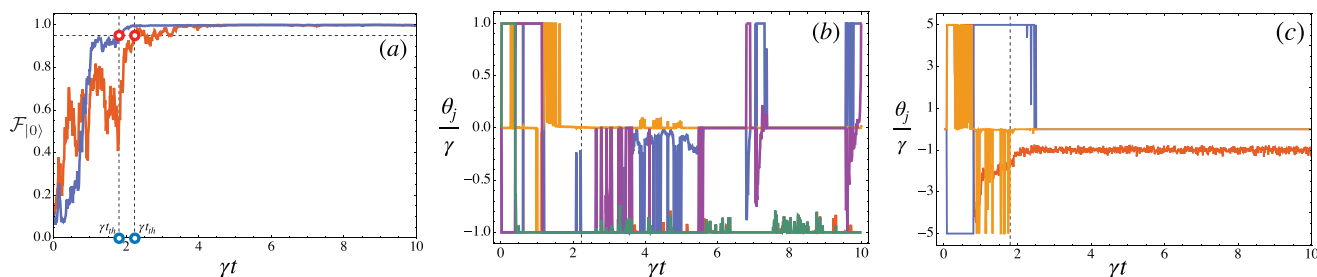


Figure 5. Single trajectory for the multiple-feedback Hamiltonian protocol with bounded domain. a) Reward function $F_{|0\rangle}(\bullet)$ as a function of time for $N = 5$, $\xi = 1$ (red line) and $N = 11$, $\xi = 5$ (blue line). In this case, we have respectively $\gamma t_{th} = 1.80$ and $\gamma t_{th} = 2.23$, highlighted by the red circles. b) Feedback couplings θ_i/γ as a function of time for the $N = 5$ trajectory: red line: θ_0 ; blue line: θ_1 ; orange line: θ_2 ; purple line: θ_3 ; green line: θ_4 . c) Feedback couplings θ_i/γ as a function of time for the $N = 11$ trajectory: Red line: θ_0 ; blue line: θ_1 ; orange line: θ_2 . All the other feedback couplings are null (apart for some numerical noise of order 10^{-8}) and we do not report them here. In (b, c) the vertical dashed line corresponds to the threshold time γt_{th} of the single trajectory. The parameters considered are $\eta = 1$ and $dt = 0.01$.

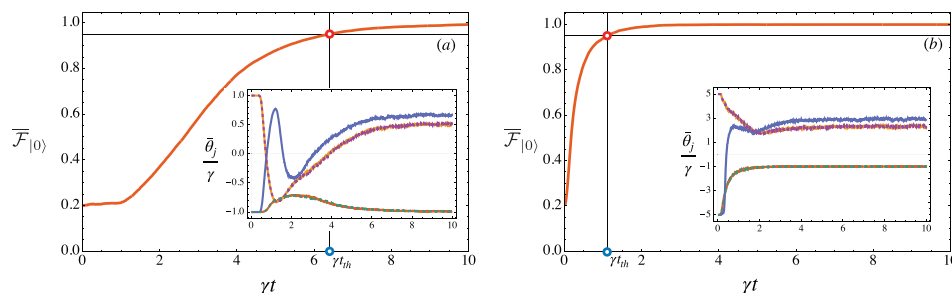


Figure 6. Digital feedback control for $N = 5$. Left panel: Three possible value of the control parameters: $\{0, \pm\gamma\}$. Right panel: Five possible value of the control parameters: $\{0, \pm\gamma, \pm\xi\gamma\}$ with $\xi = 5$. Main plot: Averaged fidelity $\bar{F}_{|0\rangle}$ as a function time. Inset: Averaged feedback couplings $\bar{\theta}_j$ as a function of time. Red line: θ_0 ; orange line: θ_1 ; blue line: θ_2 ; purple dashed line: θ_3 ; green dashed line: θ_4 . The red and the green line are superposed, as well as the orange and the purple. The number of trajectories is $N_{ij} = 5000$, and the parameters considered are $\eta = 1$ and $dt = 0.01$.

algorithm we considered in this section cannot fail, as all the possible combinations are tested.

The averaged values of the feedback couplings reported in the inset of Figure 6 show that the extra switchers are considerably used in the initial stage of the evolution. As time increases, also in this case the values of $\bar{\theta}_0$ and $\bar{\theta}_4$ reach the asymptotic value of $\bar{\theta}_0 = \bar{\theta}_4 = -\gamma$. The other couplings, instead, reach an asymptotic value larger than one and are particularly noisy. This is a sign that, in each trajectory, the walker dynamics must often be corrected by the boosted positive feedback couplings.

6. Conclusions

The ability to control or manipulate the dynamics of a quantum walker over a network is important for the development of quantum computation, quantum algorithms, and simulations. In this work we proposed a new protocol for searching a target node over a cycle graph by means of a continuous-time quantum walk. The CTQW interacts with environmental bosonic modes that are continuously monitored and then a proper feedback operation is applied to drive the walker toward the target state. The feedback thus plays the role of a dynamic oracle, able to recognize the marked vertex and to change the values of the couplings between the nodes. In this work we analyzed and compared the performances of three different feedback strategies. In the first one, we optimized the feedback couplings without posing any bound on their values; then we considered the case of bounded control, by introducing a bounding parameter ξ ; finally, we studied the case of digital feedback, where the optimal couplings were picked from a discrete set of values. We show how all the three strategies are able to localize the walker on the target node, with higher probability with respect to the quantum spatial search algorithm with a projective oracle. In particular, as expected, the minimum time necessary to reach a threshold target fidelity is lower in the unbounded case, while the continuous bounded control and the digital feedback strategies achieve similar results. Furthermore, for all considered strategies, we show that once the target vertex is reached, the feedback operates to keep the walker in this position. This is an important difference with respect to standard spatial search protocols,^[18,24] where the target is found, with higher probability, at a specific time or in a very narrow time window.

The implications are relevant, especially at the experimental and operational level, as in our protocol one does not need to perform the final position measurement at a specific time, but rather at any time larger than the known threshold.

Different physical realizations of quantum walks have been proposed in recent years. Among others, photonic realizations in integrated optical waveguide,^[84–87] single optically trapped atoms in a 1D optical lattice,^[88,89] or even with trapped ions.^[90–92] Concerning possible implementations of our scheme, we specifically mention cold-atom platforms.^[93–95] Recently it has been demonstrated how one can also achieve rapid reconfigurability of the network parameters by combination with optical tweezers.^[96] Moreover promising steps toward continuous monitoring of observables in this framework have been put forward.^[97] Instead of using an homodyne detection scheme, an alternative monitoring approach could also be modeled on the spontaneous emission observed in a Bose-Einstein condensate.^[98] Although in this paper we focus on the cycle graph, our scheme can be, in principle, generalized to more general topologies with appropriate adaptations both in the feedback operations and system dynamics that is, respectively by changing the feedback Hamiltonian and the system-environment coupling.

Appendix A: The Standard Search Algorithm in a Cycle Graph

The standard approach of quantum spatial search, using quantum walks, relies on the Hamiltonian in Equation (2), which can be rewritten as

$$H_S = \gamma L - \beta |w\rangle\langle w| \quad (\text{A1})$$

where γ scales the time (or alternatively we can set $\gamma = 1$) and β/γ is the oracle parameter that we need to optimize to improve the search. In this way, we can compare the different search strategies, by showing the dynamical quantities of interest in terms of the re-scaled time γt . If we apply this algorithm to 1D lattices, such as the cycle graph, the success probability of finding the target does not scale well with the size of the graph. In **Figure A1**, we show how the spatial search algorithm performs in the case of a cycle graph. We compare three different sizes: $N = 5, 11$, and 15 . For each graph, we numerically optimize the oracle parameter and then compute the probability of finding the target, also called reward function and defined in Equation (22), as a function of time γt . We see that for already

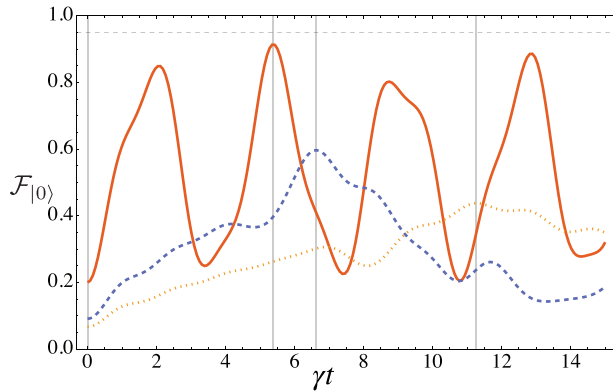


Figure A1. Reward function $F_{|0\rangle}$ for the optimized standard algorithm with the projective oracle for $N = 5$ (red line), $N = 11$ (blue dashed line), and $N = 15$ (orange dotted line). For each size N , we found the optimal value for the β parameter that gives the maximum value of $F_{|0\rangle}$ in the considered time interval. We obtain the following: for $N = 5$, $\gamma t_{opt} = 5.38$, $\beta_{opt}/\gamma = 2.24$, and the maximum is $F_{|0\rangle}(t_{opt}, \beta_{opt}) = 0.91$; for $N = 11$, $\gamma t_{opt} = 6.23$, $\beta_{opt}/\gamma = 1.19$ and the maximum is $F_{|0\rangle}(t_{opt}, \beta_{opt}) = 0.60$; for $N = 15$, $\gamma t_{opt} = 11.28$, $\beta_{opt}/\gamma = 0.92$, and the maximum is $F_{|0\rangle}(t_{opt}, \beta_{opt}) = 0.44$.

$N = 15$ the maximum probability of finding the target is less than 0.5 in the time interval considered.

Appendix B: Unconditional Master Equation and the Monitoring Operators \hat{c}_j

In this appendix, we provide some details regarding the choice of the jump operators in Equations (16) and (17). We recall that the evolution of an unconditional state is described by the following master equation

$$d\rho^u = -i\gamma[L, \rho^u(t)]dt + \kappa \sum_j D[\hat{c}_j]\rho^u(t)dt \quad (B1)$$

where $\{\hat{c}_j\}$ is the set of jump operators describing the coupling of the system's degrees of freedom with the surrounding environment, and L denotes the Laplacian operator characterizing the quantum walk defined in Section 2. Since the cycle graph is symmetric under translations of the node's index and all nodes are equivalent, we expect an unconditioned dynamics to reflect this invariance. We will show how this requirement sets some constraints in the choice of \hat{c}_j . Since our goal is to monitor the position of the walker, one may consider any operator diagonal in the position basis $\{|k\rangle\}$, such as for example

$$\hat{c}_K = \hat{K} = \sum_{k=0}^{N-1} |k\rangle\langle k| \quad (B2)$$

In this case one has that physically each node couples with the bosonic operator of the external field and this coupling is proportional to the index of the node itself. The unconditioned dynamics in Equation (B1) for an initially equally superposed state given in Equation (3) would eventually lead to a maximally mixed state at long times, as one expects. However, as we show in **Figure B1**, during the time evolution, one observes that the symmetry of the graph is lost, as the different probabilities $p_k(t) = \langle k|\rho^u(t)|k\rangle$ have different behaviors in time. The reason behind the broken symmetry is that one has to fix the node having eigenvalue $k = 0$. Indeed, with a single real jump operator diagonal in the position basis, it is not possible to have an unconditioned dynamics that preserve the cycle symmetry. There

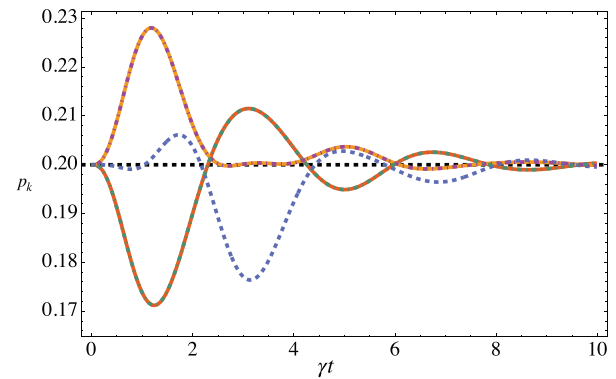


Figure B1. Time-evolution of diagonal elements of the unconditioned density matrix $p_k = \langle k|\rho^u(t)|k\rangle$ in the position basis for the unconditioned dynamics Equation (B1) in a cycle graph with $N = 5$ and $\kappa = \gamma$. Pair of jump operators \hat{c}_1 and \hat{c}_2 in Equations (16) and (17) or single non-Hermitian jump operator \hat{c}_0 in Equation (B3): black dashed line $p_0 = p_1 = p_2 = p_3 = p_4 = 1/5$. Single jump operator \hat{c}_K in Equation (B2): green dot dashed line: $p_0(t)$; red line: $p_1(t)$; purple dot dashed line: $p_2(t)$; orange line: $p_3(t)$; blue dashed line: $p_4(t)$. The initial state is the uniform superposition of all nodes of the graph as in Equation (3).

are two possible ways to circumvent this problem: the first is to consider a non-Hermitian jump operator

$$\hat{c}_0 = \sum_{k=0}^{N-1} e^{i2\pi k/N} |k\rangle\langle k| \quad (B3)$$

The second way is to use two jump operators, each diagonal in the position basis, like the one given in Equations (16)–(17). As remarked in the main text, the eigenvalues of these operators correspond to the coordinates of the nodes in the (x, y) plane.

We now discuss the evolution corresponding to the unconditional dynamics for the three choices of jump operators. In **Figure B1** we report the probabilities $p_k(t) = \langle k|\rho^u(t)|k\rangle$ of the diagonal element of the density matrix in the position basis under the master equation (Equation (B1)). We see that, both with the non-Hermitian jump operator (Equation (B3)) or with the pair of jump operators Equations (16) and (17), the probabilities $p_k(t)$ are constant in time, and thus describe a proper pure dephasing evolution, keeping the nodes populations constant and preserving the node symmetry, which instead is lost with the single jump operator in Equation (B2).

One can also show that the two unconditioned dynamics that preserve this symmetry are not equivalent. This can be seen by looking at the off diagonal elements $\rho_{ij}(t) = \langle i|\rho^u(t)|j\rangle$. In fact we first observe that the absolute values of these off-diagonal elements have an identical behavior as a function of time for the same choice of the coupling constant κ , leading to the same mixed steady-state diagonal in the position basis. However a different behavior is observed if we focus on the imaginary and real parts of these quantities. Just as an example, in **Figure B2** we report their evolution for the element $\rho_{01}(t)$. While for the pair of jump operators (\hat{c}_1, \hat{c}_2) the imaginary part is always equal to zero, and the real part decreases exponentially to zero, for the single jump operator \hat{c}_0 , one observes damped oscillations for both quantities.

In the main text we have focused on the evolution due to the pair of jump operators \hat{c}_1 and \hat{c}_2 , as their eigenvalues directly correspond to the coordinates of the walker position. In this sense one could think to be able to couple the walker to two independent environments via quantum non demolition-like interactions, in order to perform continuous monitoring of these observables. In this sense this choice is the one that, in our opinion, better fits the description in terms of continuous monitoring. However in the next appendix we show that similar results are obtained by considering

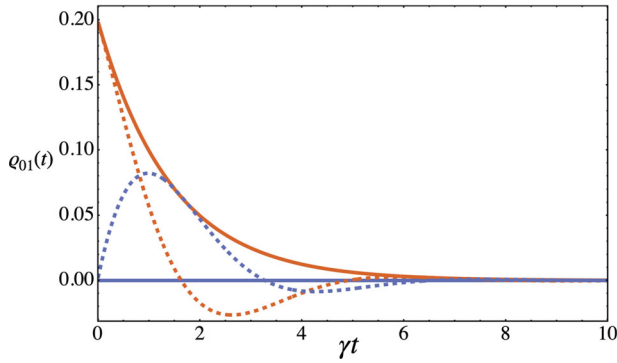


Figure B2. Real (red lines) and imaginary (blue lines) parts of the off-diagonal element $\rho_{01}(t)$ for the unconditioned dynamics Equation (B1) in a cycle graph with $N = 5$ and $\kappa = \gamma$ for the single jump operator \hat{c}_0 (dashed lines) and for the pair of jump operators (\hat{c}_1, \hat{c}_2) (solid lines). The initial state is prepared in the uniform superposition of all nodes of the graph as in Equation (3).

the dynamics with a single jump operator \hat{c}_0 and with continuous heterodyne detection.

Appendix C: Results for the Single Complex Jump Operator \hat{c}_0

In this appendix, we report the results of the bounded feedback protocol with the non-Hermitian jump operator \hat{c}_0 given in Equation (B3), analyzing the reward function in Equation (22) for a single case of study, analogously to Figure 3.

In this scenario, we can still obtain two distinct photocurrents yielding information on the position operators (\hat{x}, \hat{y}) by performing heterodyne detection instead of homodyne. In fact, in this case, one has two photocurrents given by [31, 99]

$$\begin{aligned} dY_t^{(1)} &= \sqrt{\frac{\eta\kappa}{2}} \text{Tr}[(\hat{c}_0 + \hat{c}_0^\dagger)\rho^c]dt + dW_t^{(1)} \\ &= \sqrt{2\eta\kappa} \text{Tr}[\hat{x}\rho^c]dt + dW_t^{(1)} \end{aligned} \quad (\text{C1})$$

$$\begin{aligned} dY_t^{(2)} &= \sqrt{\frac{\eta\kappa}{2}} \text{Tr}[(-i\hat{c}_0 + i\hat{c}_0^\dagger)\rho^c]dt + dW_t^{(2)} \\ &= \sqrt{2\eta\kappa} \text{Tr}[\hat{y}\rho^c]dt + dW_t^{(2)} \end{aligned} \quad (\text{C2})$$

where $dW_t^{(1)}$ and $dW_t^{(2)}$ denotes two independent Wiener increments. As explained in Section 3, the evolution of the conditional state $\rho^c(t+dt)$, described by Equation (10), is determined by a single Kraus operator, that for an heterodyne detection can be written as

$$\hat{M}_{dY_t} = \mathbb{I} - \frac{\kappa}{2} \hat{c}_0^\dagger \hat{c}_0 dt + \sqrt{\frac{\eta\kappa}{2}} \hat{c}_0 (dY_t^{(1)} - idY_t^{(2)}) \quad (\text{C3})$$

By looking at the two photocurrents, we can use the same algorithm we used in the main text to drive the walker to the target node.

In **Figure C1** we report the behavior of the average reward function for the multiple feedback Hamiltonians protocol described in Section 4 and with bounded domains. The results reported are comparable with the one obtained in Figure 3, meaning that the two protocols have similar performances. In particular we observe that the curves at fixed ξ are almost coincident, except for the case of $\xi = 1$. We may thus conjecture that in general the two strategies corresponding to the different jump operators lead to the similar results, but for small ξ and for the jump operator \hat{c}_0

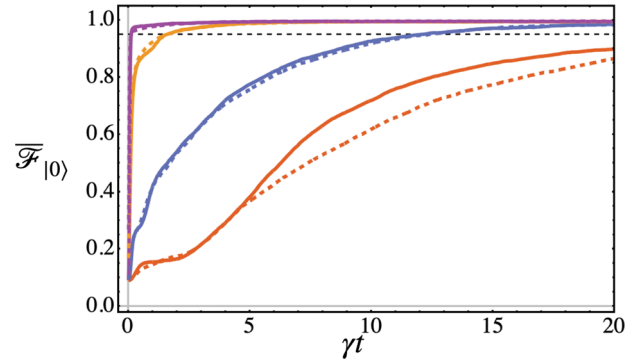


Figure C1. Comparison between the average reward function $\bar{F}_{|0\rangle}$ for multiple feedback Hamiltonians $\hat{h}_k^{(\text{hop})}$ with the single non-Hermitian jump operator \hat{c}_0 (solid) and the protocol with two jump operator (thick) already reported in Figure 3. We consider bounded control parameters θ and a graph with $N = 11$ nodes. Black dashed line: threshold $F^{\text{th}} = 0.95$. We used $\xi = 1$ (red line), $\xi = 5$ (blue line), $\xi = 50$ (orange line), $\xi = 100$ (purple line), $\kappa = \gamma$, $\eta = 1$, $\gamma dt = 0.01$, number of stochastic trajectories $N_{\text{ij}} = 5000$.

the algorithm implemented does not find the optimal feedback strategy, leading to smaller values of the average fidelity.

Appendix D: Shape of the Landscape of the Reward Function $F_{|0\rangle}$

In this section, we discuss some details regarding the landscape of the reward function $F_{|0\rangle}$ for the protocol used in the main text, that is, with the pair of jump operators given in Equations (16) and (17). The aim is to provide a heuristic argument for the large fluctuations we observe in the average feedback couplings in the unbounded domain, (see Figure 2).

The landscape is, by definition, a function of the domain of the reward function (which is \mathbb{R}^N , with N is the size of the cycle graph, i.e., the number of feedback couplings); for this reason it is not possible to plot the full landscape even for the smallest case we considered, that is, $N = 5$. Nonetheless, driven by the numerical results obtained in the main text and by symmetry considerations, we can restrict the domain in our analysis. Considering the notation of Figure 1, we can assume that $\theta_0 = \theta_4$ and $\theta_1 = \theta_3$, as confirmed by the results shown in Figure 2, where we can clearly see this symmetry, up to some fluctuations. We further assume that $\theta_2 = 0$, which is supported by numerical results in both the unbounded and bounded case, even though we did not report them explicitly in the main text. In this way, we can now picture the landscape as a 3D function with two free feedback couplings, θ_0 and θ_1 .

The landscapes for a single trajectory and at different times are reported in **Figure D1**, with $N = 5$ and $\xi = 1$, which is the smallest domain we have studied. Please, notice that the landscape in the figure is plotted for a larger domain, that is, $\{\theta_0/\gamma, \theta_1/\gamma\} \in \{[-10, 10], [-10, 10]\}$. This means that the bounded algorithm is going to pick values in a smaller square centered in the 3D plots we have reported. We show this larger domain to illustrate why smaller domains (i.e., smaller ξ) leads to a slower increase of the average fidelity: one indeed observes that the maxima of the reward function are not accessible if ξ is smaller than a certain threshold. We also stress that the algorithm that drives the walker does not assume that the angles are equal, that is, $\theta_0 = \theta_4$ and $\theta_1 = \theta_3$ and $\theta_2 = 0$.

The landscapes reported in Figure D1 show an oscillatory shape without a single global maximum but with many local maxima with the same height. This means that when the domain is enlarged (or even unbounded), at each step the algorithm might find a maximum outside the neighborhood of the maximum found at the previous step. In the case of an unbounded domain, the periodicity of the landscape allows the algo-

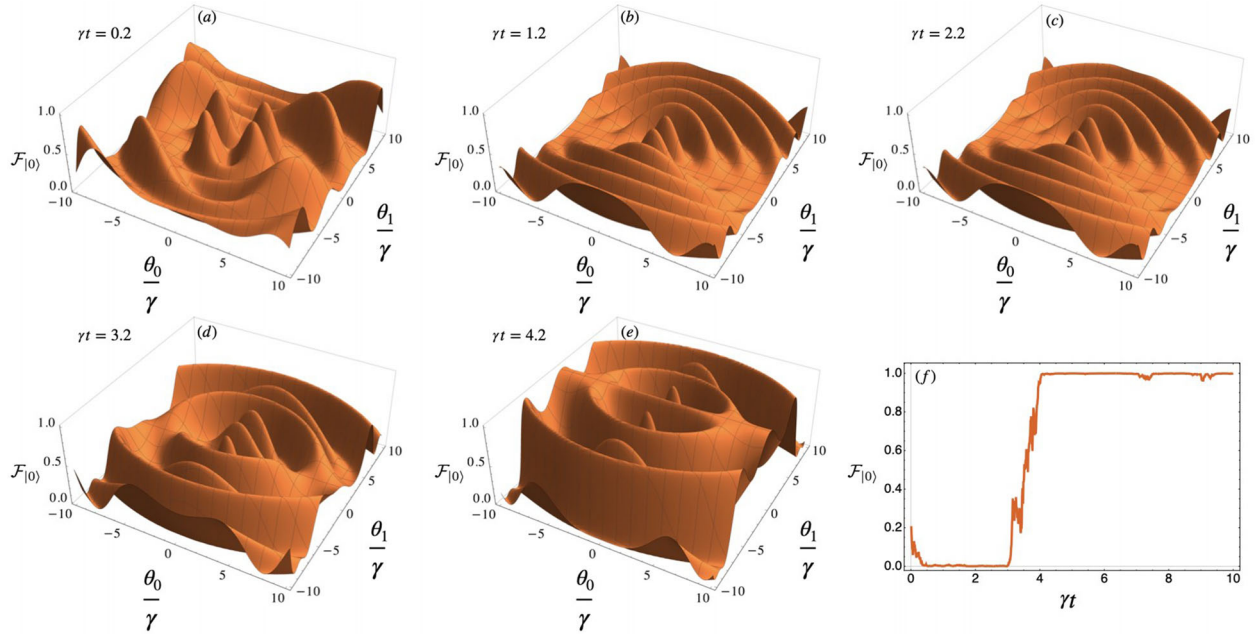


Figure D1. Landscapes for the reward function $F_{|0\rangle}$ in a single trajectory at different time step. Panels (a)–(e) are the landscapes, panel (f) is the evolution of the reward function as a function of γt . Comparing the two, we see the changes in the landscape as soon as the reward function increase. The parameters considered are $N = 5$, $\xi = 1$, $\kappa = \gamma$, $\gamma dt = 0.01$, and $\eta = 1$. Please notice that the algorithm see only a smaller square of the values reported, as explained in Appendix D.

algorithm to find maxima at very large values of the feedback coupling, which gives rise to the large fluctuations in the average feedback couplings in Figure 2. To circumvent the problem, one could consider an algorithm in which, at each step, the feedback couplings are allowed to change in a small neighborhood around the optimal value found at the previous step. We leave this to future investigations but we believe that this protocol should not substantially change the performance of the one used but should solve the large fluctuations problem we have observed.

Appendix E: Unitary Feedback: Analytic Expression of the Feedback Couplings θ

In this appendix we provide a detailed and analytical derivation for the expression of the feedback couplings in the case of a single feedback Hamiltonian, assuming that they are of the order of dt and dW_i , by following the results presented in ref. [45]. In the interaction picture, the conditioned evolution for the density matrix due to d_M measurements is given by Equation (6), and can be recasted as

$$\begin{aligned} \rho^c(t+dt) = & \rho^c(t) + \sqrt{\kappa} \sum_{i=1}^{d_M} H[\hat{c}_i] \rho^c(t) dW_i \\ & + \sum_{i=1}^{d_M} \kappa D[\hat{c}_i] \rho^c(t) dt \end{aligned} \quad (E1)$$

where the superoperator $D[\hat{c}_i] \bullet$ and $H[\hat{c}_i] \bullet$ are defined in Equations (7) and (8), respectively.

As explained in the Section 4, our feedback Hamiltonian is identified with the adjacency matrix (1), that is

$$\hat{H}_{fb}(\theta) = \theta \sum_{i=0}^{N-1} \hat{h}_i^{(\text{hop})} \quad (E2)$$

with $\hat{h}_i^{(\text{hop})}$ defined in Equation (21). The single-feedback Hamiltonian protocol proposed here is nothing but the multiple-feedback protocol in which the single couplings change synchronously and with equal strength. Here

we assume that the expression for the feedback coupling θ for the step $t + dt$ can be expanded as

$$\bar{\theta} = \theta dt = \sum_{k=1}^2 A_k dW_t^{(k)} + B dt \quad (E3)$$

with $A = \{A_1, A_2\}$ and B are respectively a 2D real vector and a real number. Then, the unitary evolution due to the feedback can be written as

$$\begin{aligned} \hat{U} = & \exp \left\{ -i \hat{H}_{fb}(\theta) dt \right\} \\ = & \exp \left\{ -i \hat{h}_{fb} \sum_{k=1}^2 A_k dW_t^{(k)} - i \hat{h}_{fb} B dt \right\} \end{aligned} \quad (E4)$$

$$= \exp \left\{ -i \hat{h}_{fb} \sum_{k=1}^2 A_k dW_t^{(k)} - i \hat{h}_{fb} B dt \right\} \quad (E5)$$

where we have introduced the operator $\hat{h}_{fb} = \sum_{i=0}^{N-1} \hat{h}_i^{(\text{hop})}$. The Taylor expansion of such operator up to first order in dt is obtained

$$\hat{U} = \mathbb{I} - i \hat{h}_{fb} \sum_{k=1}^2 A_k dW_t^{(k)} - i \hat{h}_{fb} B dt + \quad (E6)$$

$$- \frac{1}{2} \hat{h}_{fb}^2 \sum_{k=1}^2 A_i^2 dt \quad (E7)$$

From the latter expression, we can derive the infinitesimal evolution after the feedback (remember that $dW_t^{(i)} dW_t^{(j)} = dt \delta_{ij}$)

$$\begin{aligned} \rho_\theta^f(t+dt) = & \hat{U} \rho^c(t+dt) \hat{U}^\dagger = \rho_\theta^f(t) + \sqrt{\kappa} \sum_{i=1}^2 H[\hat{c}_i] \rho_\theta^f(t) dW_t^{(i)} \\ & + \kappa \sum_{i=1}^2 D[\hat{c}_i] \rho_\theta^f(t) dt - i [\hat{h}_{fb}, \rho_\theta^f(t)] \sum_{i=1}^2 A_i dW_t^{(i)} + \end{aligned} \quad (E8)$$

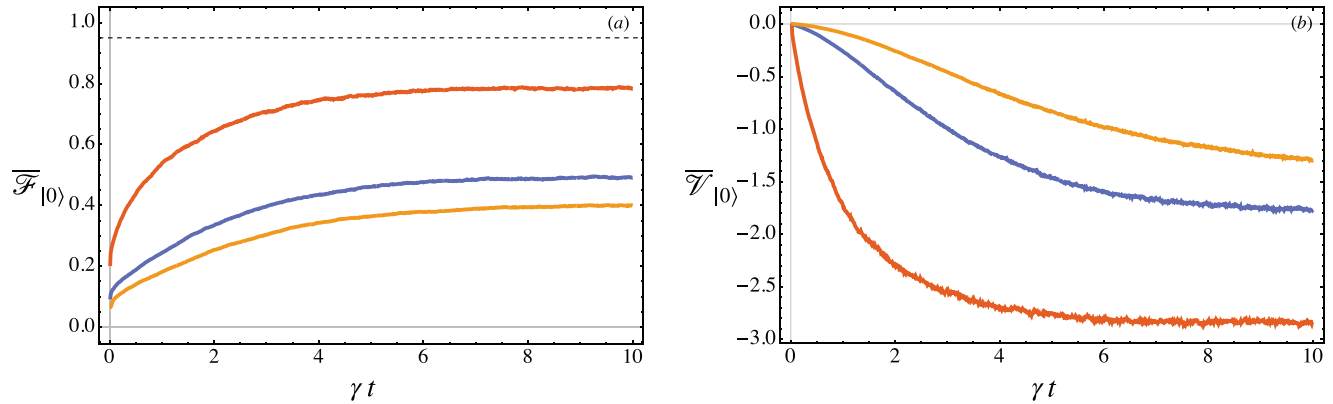


Figure E1. Single-feedback Hamiltonian protocol with \hat{H}_F defined in Equation (E2) for $N_{ij} = 5000$ trajectories and parameters $\eta = \kappa = 1$ and $dt = 0.01$. a) Average reward function $\bar{F}_{|0\rangle}$ with respect to the target state as a function of time t . Dashed line: threshold fidelity F_{th} . b) Average of the second derivative \bar{V} defined in Equation (E16) as a function of time t . Red line $N = 5$; blue line $N = 11$; orange line $N = 15$.

$$-i\sqrt{\kappa}[\hat{h}_{fb}, H[\hat{c}_i]\hat{\sigma}_\theta^f(t)] \sum_{i=1}^2 A_i dt - i[\hat{h}_{fb}, \hat{\sigma}_\theta^f(t)] B dt + \sum_{i=1}^2 A_i^2 D[\hat{h}_{fb}]\hat{\sigma}_\theta^f(t) dt = \quad (E9)$$

$$= \hat{\sigma}_\theta^f(t) + \sum_{i=1}^2 \hat{\mathcal{W}}_i dW_t^{(i)} + \left(\sum_{i=1}^2 \hat{\mathcal{T}}_i - i[\hat{h}_{fb}, \hat{\sigma}_\theta^f(t)] \right) B dt \quad (E10)$$

where we have grouped the differential factors together, that is,

$$\hat{\mathcal{W}}_i = \sqrt{\kappa} H[\hat{c}_i]\hat{\sigma}_\theta^f(t) - iA_i[\hat{h}_{fb}, \hat{\sigma}_\theta^f(t)] \quad (E11)$$

$$\hat{\mathcal{T}}_i = \kappa D[\hat{c}_i]\hat{\sigma}_\theta^f(t) - i\sqrt{\kappa} A_i[\hat{h}_{fb}, H[\hat{c}_i]\hat{\sigma}_\theta^f(t)] \quad (E12)$$

$$+ A_i^2 D[\hat{h}_{fb}]\hat{\sigma}_\theta^f(t) \quad (E12)$$

To obtain the value of A and B which determines the feedback operation at each time-step, we require that the derivative of the linear reward function $\Lambda(\rho(t))$ with respect to θ at the following time step of the evolution

$$G(t+dt) = \frac{\partial}{\partial \theta} \left(\Lambda(\hat{\sigma}_\theta^f(t+dt)) \right) \Big|_{\hat{\theta}=\hat{\theta}_{opt}} = \quad (E13)$$

$$= \Lambda \left(\frac{\partial}{\partial \theta} \hat{\sigma}_\theta^f(t+dt) \Big|_{\hat{\theta}=\hat{\theta}_{opt}} \right) \quad (E14)$$

satisfy the extremality condition

$$G(t+dt) = 0 \quad (E15)$$

In addition, since we are interested in maximizing $\Lambda(\bullet)$, we ask also that the second derivative of the reward function is negative, that is,

$$V = \Lambda \left(\frac{\partial^2 \hat{\sigma}_\theta^f(t+dt)}{\partial \theta^2} \Big|_{\hat{\theta}=\hat{\theta}_{opt}} \right) < 0 \quad (E16)$$

which ensures that the feedback operation maximize the reward function. To find the solution, we first evaluate

$$\partial_\theta \hat{\sigma}_\theta^f(t+dt) = i[\hat{H}_{fb}(\theta), \hat{\sigma}_\theta^f(t+dt)] \quad (E17)$$

Then, the condition in Equation (E15) can be expanded as follows

$$G(t+dt) = -i\Lambda([\hat{h}_{fb}, \hat{\sigma}_\theta^f(t)]) - i \sum_{j=1}^2 \Lambda([\hat{h}_{fb}, \hat{\mathcal{W}}_j]) dW_t^{(j)} - i \left(\sum_{j=1}^2 \Lambda([\hat{h}_{fb}, \hat{\mathcal{T}}_j]) - iB\Lambda([\hat{h}_{fb}, [\hat{h}_{fb}, \hat{\sigma}_\theta^f(t)]]) \right) dt \quad (E18)$$

Now, the first term in the latter equation is null since we assume that at the previous time step the reward function satisfy the extremality condition. Then, considering the terms proportional to dW_t^j we have that for $j = 1, 2$ $\Lambda([\hat{h}_{fb}, \hat{\mathcal{W}}_j]) = 0$, which is nothing but

$$A_j = -i\sqrt{\kappa} \frac{\langle 0 | [\hat{h}_{fb}, H[\hat{c}_j]\hat{\sigma}_\theta^f(t)] | 0 \rangle}{\langle 0 | [\hat{h}_{fb}, [\hat{h}_{fb}, \hat{\sigma}_\theta^f(t)]] | 0 \rangle} \quad (E19)$$

where we have considered as reward function the one defined in Equation (22), that is, $\Lambda(\bullet) = \langle 0 | \bullet | 0 \rangle$. With the same line of reasoning, taking the term proportional to dt we can obtain the scalar function

$$B = -i \frac{\sum_{j=1}^2 \langle 0 | [\hat{h}_{fb}, \hat{\mathcal{T}}_j] | 0 \rangle}{\langle 0 | [\hat{h}_{fb}, [\hat{h}_{fb}, \hat{\sigma}_\theta^f(t)]] | 0 \rangle} \quad (E20)$$

We notice that these equations are valid if $\langle 0 | [\hat{h}_{fb}, [\hat{h}_{fb}, \hat{\sigma}_\theta^f(t)]] | 0 \rangle \neq 0$, a condition that must be checked at each step of the feedback operation.

In addition, the condition for maximizing the reward function at each time step certain time can be simply written as

$$V_{|0\rangle}(t+dt) = -i[\hat{h}_{fb}, [\hat{h}_{fb}, \hat{\sigma}_\theta^f(t+dt)]] < 0 \quad (E21)$$

If this condition fails, we chose not to act with the feedback operation and skip to the next time-step, even though numerical evidence shows that this situation rarely occurs.

The numerical results of this protocol are reported in **Figure E1**, left panel. The average fidelity $\bar{F}_{|0\rangle}$ for $N_{ij} = 5000$ trajectories for three different values of $N = 5, 11$, and 15 . As the size increases, the efficiency of the protocol worsens. Moreover, it never reaches the threshold value $\bar{F}_{|0\rangle}^{th}$.

In the right panel of Figure E1 we report the average value of the second derivative, that is, $\bar{V}_{|0\rangle} = E_{\text{traj}}[V_{|0\rangle}(t+dt)]$. The results obtained show that

the feedback operation is always optimal *on average* at each time step. However, since the threshold value $\overline{F}_{|0\rangle}^{\text{th}}$ is never reached, we conclude that the single-feedback Hamiltonian is inefficient in achieving the targeting goal, even though the θ found according to Equations (E19) and (E20) to be the optimal one. In addition, the absolute values of \mathcal{V} decrease as N increases, showing that the efficiency of the protocol worsens as the size increases, as we have already observed in the main text for the multi-coupling feedback Hamiltonian.

Acknowledgements

The authors acknowledge useful discussion with Francesco Albarelli. M.G.A.P. is a member of INDAM-GNFM.

Conflict of Interest

The authors declare no conflict of interest.

Data Availability Statement

The data that support the findings of this study are available from the corresponding author upon reasonable request.

Keywords

continuous measurement, continuous-time quantum walks, network search, quantum control, quantum feedback, quantum search

Received: July 29, 2022
Revised: October 12, 2022
Published online:

- [1] E. Farhi, S. Gutmann, *Phys. Rev. A* **1998**, 58, 915.
- [2] J. Kempe, *Contemp. Phys.* **2003**, 44, 307.
- [3] S. E. Venegas-Andraca, *Quantum Inf. Process.* **2012**, 11, 1015.
- [4] A. M. Childs, *Phys. Rev. Lett.* **2009**, 102, 180501.
- [5] V. Kendon, *AIP Conf. Proc.* **2014**, 1633, 177.
- [6] A. P. Hines, P. C. E. Stamp, *Phys. Rev. A* **2007**, 75, 062321.
- [7] A. M. Childs, E. Farhi, S. Gutmann, *Quantum Inf. Proc.* **2002**, 1, 35.
- [8] A. M. Childs, R. Cleve, E. Deotto, E. Farhi, S. Gutmann, D. A. Spielman, in *Proc. of the Thirty-Fifth Annual ACM Symp. on Theory of Computing*, STOC '03, Association for Computing Machinery, New York, NY **2003**, pp. 59–68.
- [9] J. K. Gamble, M. Friesen, D. Zhou, R. Joynt, S. N. Coppersmith, *Phys. Rev. A* **2010**, 81, 052313.
- [10] L. Rossi, A. Torsello, E. R. Hancock, *Phys. Rev. E* **2015**, 91, 022815.
- [11] C. Cade, A. Montanaro, A. Belovs, *Quantum Inf. Comput.* **2018**, 18, 18.
- [12] A. Callison, N. Chancellor, F. Mintert, V. Kendon, *New J. Phys.* **2019**, 21, 123022.
- [13] S. Marsh, J. B. Wang, *Phys. Rev. Res.* **2020**, 2, 023302.
- [14] A. Kryukov, R. Abramov, L. E. Fedichkin, A. Alodjants, A. A. Melnikov, *Phys. Rev. A* **2022**, 105, 022208.
- [15] A. Ambainis, *Int. J. Quantum Inf.* **2003**, 1, 507.
- [16] K. Kadian, S. Garhwal, A. Kumar, *Comput. Sci. Rev.* **2021**, 41, 100419.
- [17] S. E. Venegas-Andraca, *Quantum Walks for Computer Scientists*, Synthesis Lectures on Quantum Computing, Morgan & Claypool Publishers, San Rafael **2008**.
- [18] A. M. Childs, J. Goldstone, *Phys. Rev. A* **2004**, 70, 022314.
- [19] J. Janmark, D. A. Meyer, T. G. Wong, *Phys. Rev. Lett.* **2014**, 112, 210502.
- [20] A. M. Childs, Y. Ge, *Phys. Rev. A* **2014**, 89, 052337.
- [21] S. Chakraborty, L. Novo, J. Roland, *Phys. Rev. A* **2020**, 102, 022227.
- [22] M. G. A. Paris, C. Benedetti, S. Olivares, *Symmetry* **2021**, 13, 96.
- [23] C. Benedetti, D. Tamascelli, M. G. A. Paris, A. Crespi, *Phys. Rev. Appl.* **2021**, 16, 054036.
- [24] R. Portugal, *Quantum Walks and Search Algorithms*, Springer Nature Switzerland, AG **2018**.
- [25] P. J. Pemberton-Ross, A. Kay, *Phys. Rev. Lett.* **2011**, 106, 020503.
- [26] C. Chudzik, F. W. Strauch, *Phys. Rev. Lett.* **2010**, 105, 260501.
- [27] S. Paganelli, S. Lorenzo, T. J. G. Apollaro, F. Plastina, G. L. Giorgi, *Phys. Rev. A* **2013**, 87, 062309.
- [28] M. Christandl, N. Datta, T. C. Dorlas, A. Ekert, A. Kay, A. J. Landahl, *Phys. Rev. A* **2005**, 71, 032312.
- [29] A. Kay, *Int. J. Quantum Inf.* **2010**, 08, 641.
- [30] D. Tamascelli, S. Olivares, S. Rossotti, R. Osellame, M. G. A. Paris, *Sci. Rep.* **2016**, 6, 26054.
- [31] H. M. Wiseman, G. J. Milburn, *Quantum Measurement and Control*, Cambridge University Press, New York **2010**.
- [32] H. M. Wiseman, G. J. Milburn, *Phys. Rev. Lett.* **1993**, 70, 548.
- [33] H. M. Wiseman, *Phys. Rev. A* **1994**, 49, 2133.
- [34] A. C. Doherty, K. Jacobs, *Phys. Rev. A* **1999**, 60, 2700.
- [35] L. K. Thomsen, S. Mancini, H. M. Wiseman, *Phys. Rev. A* **2002**, 65, 061801.
- [36] A. Serafini, S. Mancini, *Phys. Rev. Lett.* **2010**, 104, 220501.
- [37] A. Szorkovszky, A. C. Doherty, G. I. Harris, W. P. Bowen, *Phys. Rev. Lett.* **2011**, 107, 213603.
- [38] M. G. Genoni, S. Mancini, A. Serafini, *Phys. Rev. A* **2013**, 87, 042333.
- [39] M. G. Genoni, J. Zhang, J. Millen, P. F. Barker, A. Serafini, *New J. Phys.* **2015**, 17, 073019.
- [40] S. G. Hofer, K. Hammerer, *Phys. Rev. A* **2015**, 91, 033822.
- [41] L. Martin, F. Motzoi, H. Li, M. Sarovar, K. B. Whaley, *Phys. Rev. A* **2015**, 92, 062321.
- [42] L. Martin, M. Sayrafi, K. B. Whaley, *Quantum Sci. Technol.* **2017**, 2, 044006.
- [43] L. Martin, M. Sayrafi, B. Whaley, in *Proc. Quantum Information and Measurement (QIM) 2017*, Optical Society of America, Washington, D.C. **2017**, p. QF6C.3.
- [44] M. Brunelli, D. Malz, A. Nunnenkamp, *Phys. Rev. Lett.* **2019**, 123, 093602.
- [45] L. S. Martin, *arXiv:2004.09766*, **2020**.
- [46] Y. Jiang, X. Wang, L. Martin, K. B. Whaley, *Phys. Rev. A* **2020**, 102, 022612.
- [47] S. Zhang, L. S. Martin, K. B. Whaley, *Phys. Rev. A* **2020**, 102, 062418.
- [48] M. A. C. Rossi, F. Albarelli, D. Tamascelli, M. G. Genoni, *Phys. Rev. Lett.* **2020**, 125, 200505.
- [49] A. Di Giovanni, M. Brunelli, M. G. Genoni, *Phys. Rev. A* **2021**, 103, 022614.
- [50] M. Rossi, D. Mason, J. Chen, Y. Tsaturyan, A. Schliesser, *Nature* **2018**, 563, 53.
- [51] L. Magrini, P. Rosenzweig, C. Bach, A. Deutschmann-Olek, S. G. Hofer, S. Hong, N. Kiesel, A. Kugi, M. Aspelmeyer, *Nature* **2021**, 595, 373.
- [52] F. Tebbenjohanns, M. L. Mattana, M. Rossi, M. Frimmer, L. Novotny, *Nature* **2021**, 595, 378.
- [53] T. G. Wong, L. Tarrataca, N. Nahimov, *Quantum Inf. Process.* **2016**, 15, 4029.
- [54] D. Lu, J. D. Biamonte, J. Li, H. Li, T. H. Johnson, V. Bergholm, M. Faccin, Z. Zimborás, R. Laflamme, J. Baugh, S. Lloyd, *Phys. Rev. A* **2016**, 93, 042302.
- [55] J. Turner, J. Biamonte, *J. Phys. A: Math. Theor.* **2021**, 54, 235301.
- [56] M. Frigerio, C. Benedetti, S. Olivares, M. G. A. Paris, *Phys. Rev. A* **2021**, 104, L030201.

- [57] M. Frigerio, C. Benedetti, S. Olivares, M. G. A. Paris, *Phys. Rev. A* **2022**, 105, 032425.
- [58] E. Farhi, S. Gutmann, *Phys. Rev. A* **1998**, 57, 2403.
- [59] S. Chakraborty, L. Novo, A. Ambainis, Y. Omar, *Phys. Rev. Lett.* **2016**, 116, 100501.
- [60] P. Philipp, L. Tarrataca, S. Boettcher, *Phys. Rev. A* **2016**, 93, 032305.
- [61] W. T. G., *J. Phys. A: Math. Theor.* **2016**, 49, 195303.
- [62] S. Chakraborty, L. Novo, S. Di Giorgio, Y. Omar, *Phys. Rev. Lett.* **2017**, 119, 220503.
- [63] T. G. Wong, K. Wünscher, J. Lockhart, S. Severini, *Phys. Rev. A* **2018**, 98, 012338.
- [64] Y. Wang, S. Wu, W. Wang, *Phys. Rev. A* **2020**, 101, 062333.
- [65] S. Chakraborty, L. Novo, J. Roland, *Phys. Rev. A* **2020**, 102, 032214.
- [66] I. Foulger, S. Gnutzmann, G. Tanner, *Phys. Rev. Lett.* **2014**, 112, 070504.
- [67] K. Jacobs, D. A. Steck, *Contemp. Phys.* **2006**, 47, 279.
- [68] T. A. Brun, *Am. J. Phys.* **2002**, 70, 719.
- [69] K. W. Murch, S. J. Weber, C. Macklin, I. Siddiqi, *Nature* **2013**, 502, 211.
- [70] M. Naghiloo, N. Foroozani, D. Tan, A. Jadbabaie, K. W. Murch, *Nat. Commun.* **2016**, 7, 11527.
- [71] S. Hacohe-Gourgy, L. S. Martin, E. Flurin, V. V. Ramasesh, K. B. Whaley, I. Siddiqi, *Nature* **2016**, 538, 491.
- [72] Q. Ficheux, S. Jezouin, Z. Leghtas, B. Huard, *Nat. Commun.* **2018**, 9, 1926.
- [73] Z. K. Mineev, S. O. Mundhada, S. Shankar, P. Reinhold, R. Gutiérrez-Jáuregui, R. J. Schoelkopf, M. Mirrahimi, H. J. Carmichael, M. H. Devoret, *Nature* **2019**, 570, 200.
- [74] W. Wiecek, S. G. Hofer, J. Hoelscher-Obermaier, R. Riedinger, K. Hammerer, M. Aspelmeyer, *Phys. Rev. Lett.* **2015**, 114, 223601.
- [75] M. Rossi, D. Mason, J. Chen, Y. Tsaturyan, A. Schliesser, *Nature* **2018**, 563, 53.
- [76] M. Rossi, D. Mason, J. Chen, A. Schliesser, *Phys. Rev. Lett.* **2019**, 123, 163601.
- [77] L. Magrini, P. Rosenzweig, C. Bach, A. Deutschmann-Olek, S. G. Hofer, S. Hong, N. Kiesel, A. Kugi, M. Aspelmeyer, *Nature* **2021**, 595, 373.
- [78] F. Tebbenjohanns, M. L. Mattana, M. Rossi, M. Frimmer, L. Novotny, *Nature* **2021**, 595, 378.
- [79] P. Rouchon, *arXiv:1407.7810*, **2015**.
- [80] P. Rouchon, J. F. Ralph, *Phys. Rev. A* **2015**, 91, 012118.
- [81] D. Risté, L. DiCarlo, *arXiv:1508.01385 [cond-mat, physics:quant-ph]* **2015**.
- [82] <https://docs.scipy.org/doc/scipy/reference/generated/scipy.optimize.minimize.html>.
- [83] M. Cattaneo, M. A. C. Rossi, M. G. A. Paris, S. Maniscalco, *Phys. Rev. A* **2018**, 98, 052347.
- [84] H. B. Perets, Y. Lahini, F. Pozzi, M. Sorel, R. Morandotti, Y. Silberberg, *Phys. Rev. Lett.* **2008**, 100, 170506.
- [85] A. Peruzzo, M. Lobino, J. C. Matthews, N. Matsuda, A. Politi, K. Poulios, X.-Q. Zhou, Y. Lahini, N. Ismail, K. Wörhoff, Y. Bromberg, Y. Silberberg, M. G. Thompson, J. L. O'Brien, *Science* **2010**, 329, 1500.
- [86] M. Gräfe, R. Heilmann, M. Lebugle, D. Guzman-Silva, A. Perez-Leija, A. Szameit, *J. Opt.* **2016**, 18, 103002.
- [87] Z.-Q. Jiao, J. Gao, W.-H. Zhou, X.-W. Wang, R.-J. Ren, X.-Y. Xu, L.-F. Qiao, Y. Wang, X.-M. Jin, *Optica* **2021**, 8, 1129.
- [88] M. Karski, L. Förster, J.-M. Choi, A. Steffen, W. Alt, D. Meschede, A. Widera, *Science* **2009**, 325, 174.
- [89] M. Genske, W. Alt, A. Steffen, A. H. Werner, R. F. Werner, D. Meschede, A. Alberti, *Phys. Rev. Lett.* **2013**, 110, 190601.
- [90] F. Zähringer, G. Kirchmair, R. Gerritsma, E. Solano, R. Blatt, C. F. Roos, *Phys. Rev. Lett.* **2010**, 104, 100503.
- [91] H. Schmitz, R. Matjeschk, C. Schneider, J. Glueckert, M. Enderlein, T. Huber, T. Schaetz, *Phys. Rev. Lett.* **2009**, 103, 090504.
- [92] P. Xue, B. C. Sanders, D. Leibfried, *Phys. Rev. Lett.* **2009**, 103, 183602.
- [93] U. Schneider, L. Hackermüller, J. P. Ronzheimer, S. Will, S. Braun, T. Best, I. Bloch, E. Demler, S. Mandt, D. Rasch, A. Rosch, *Nat. Phys.* **2012**, 8, 213.
- [94] P. M. Preiss, R. Ma, M. E. Tai, A. Lukin, M. Rispoli, P. Zupancic, Y. Lahini, R. Islam, M. Greiner, *Science* **2015**, 347, 1229.
- [95] E. J. Meier, F. A. An, B. Gadway, *Phys. Rev. A* **2016**, 93, 051602.
- [96] A. W. Young, W. J. Eckner, N. Schine, A. M. Childs, A. M. Kaufman, *Science* **2022**, 377, 885.
- [97] C. Laflamme, D. Yang, P. Zoller, *Phys. Rev. A* **2017**, 95, 043843.
- [98] J. Clark, C. Groiseau, Z. Shaw, S. Dadras, C. Binégay, S. Wimberger, G. Summy, Y. Liu, *Phys. Rev. Res.* **2021**, 3, 043062.
- [99] M. G. Genoni, S. Mancini, A. Serafini, *Russ. J. Math. Phys.* **2014**, 21, 329.